Control strategies for order–disorder phase transition in crowd evacuation

Wenfeng Yi [a] , Wenhan Wu [b],*

[a] *College of Artificial Intelligence, China University of Petroleum, Beijing 102249, China*
[b] *Senseable City Laboratory, Massachusetts Institute of Technology, Cambridge, MA 02139, USA*

ARTICLE INFO

ABSTRACT

Crowd evacuation can undergo abrupt, hazardous shifts between ordered and disordered motion, yet how network topology and targeted interventions jointly shape this transition remains unclear. We integrate a dynamic, weighted small-world contagion layer with an extended social force model and design adaptive, topology-aware interventions that target high-degree (HD) and high k-shell (HK) nodes. Simulations map a risk-induced transition: low risk permits spontaneous recovery, medium risk triggers a critical collapse of alignment, and high risk locks the system into disorder. Targeting a small fraction of agents (10%–20%) lowers collective impatience and preserves alignment, with HD retaining more benefit at higher densities. In dual-exit rooms under high risk — where a short random-walk disorientation rule and a pressure–emotion coupling are active — raising alignment via targeted control reduces evacuation time, re-balances exit usage, and lowers peak contact forces. These effects remain robust across exit-width changes, increases in the long-range contagion probability $p(t)$, and moderate inter-individual heterogeneity. Analyses of real crowd recordings further show that HD and HK selections overlap only partially, supporting dynamic, hybrid policies that cover both dense cores and structural bridges. Together, the results provide a topology-aware control framework that links network structure to emergent evacuation behavior, with direct implications for planning, public safety, and crowd resilience.

1. Introduction

Phase transitions, abrupt and collective shifts from disordered to ordered configurations, are ubiquitous in active matter, ranging from vibrated granular disks that spontaneously flock into moving bands [1] to bacterial swarms that organize into coherent vortices once a critical density is exceeded [2]. In animal societies, fish schools switch between milling and polarized states depending on group speed or external perturbations, while cells [3], starlings [4], locusts [5], and other species exhibit similar order–disorder transitions driven by local interactions. Theoretical insights into these phenomena have been provided by the Vicsek model and its extensions [6,7], whose flocking transition and still-debated universality class support much of modern active-matter physics. Besides, human crowds are no exception: controlled experiments in exits and multidirectional flows reveal lane formation and queuing as hallmarks of an order–disorder transition, with disordered states significantly reducing pedestrian speeds [8]. Understanding the mechanisms that govern the analogous transition from chaos to order during evacuation is therefore crucial for forecasting critical crowd conditions and designing proactive control strategies in complex environments [9].

The research of crowd dynamics has rapidly progressed in recent years, driven by rich sensing data and increasingly powerful simulation frameworks. A series of reviews make it clear that current models can no longer be grouped into a single paradigm but instead range from fluid-like continuum descriptions to psychologically grounded agent systems [10,11]. These models have explained certain empirical phenomena such as stop-and-go waves, lane formation, and arching at exits, but still leave important behavioral subtleties unresolved. Macroscopic approaches treat pedestrians as a compressible medium and adapt tools from traffic flow or granular physics [12]. Such models can reproduce large-scale congestion patterns and allow rapid optimization of building layouts, but they average out heterogeneity in intention and perception [13,14]. Microscopic models adopt the form of social force model: individuals follow self-driven desires, avoid obstacles, and exchange repulsive or attractive interactions with neighbors, which collectively reproduce various phenomena of real crowds [15,16]. A recent variant introduced biomechanical contact rules and micro-mobility devices, extending the framework to shared urban spaces [17]. A parallel line of work integrated leadership and demonstrated experimentally that a few informed agents can lead a crowd toward safer escape paths and shorten clearance times [18].
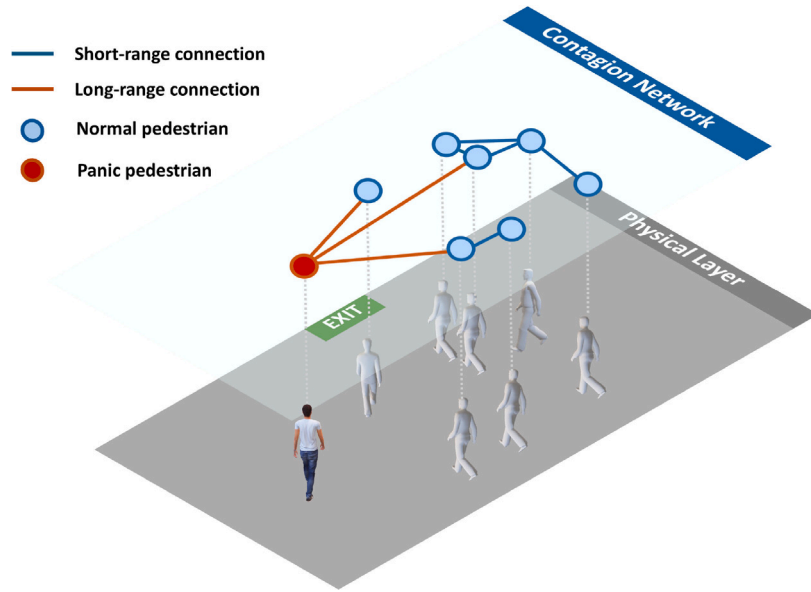
---

* Corresponding author.
E-mail address: wenhanwu@mit.edu (W. Wu).

Fig. 1. Two-layer schematic. The physical layer governs motion, while a time-varying *contagion network* carries emotional influence. Short-range proximity links are shown in blue; long-range shortcuts (orange) represent occasional rewiring. Blue nodes denote calm pedestrians; the red node is a panic seed establishing long-range contacts.

Behavior is further complicated by emotional contagion, as panic can spread faster than most physical cues and transform orderly flow into disorder in seconds. There are two principal modeling concepts: Thermodynamic-type models regard arousal as a diffusive field, and the ASCRIBE series remains influential [19,20]. In contrast, contagion-type models instead map epidemiological state transitions into contact graphs using thresholds or probabilistic infection rules [21,22]. An empirical validation indicated that an agent-based contagion model calibrated on evacuation video can predict the timing and amplitude of collective panic peaks [23], while a recent research highlighted the necessity to couple contagion dynamics with realistic movements [24].

Recent years have seen increasing efforts to model evacuation under high-stress scenarios. Guo et al. [25] combined cellular automata with social force effects to simulate how panic-induced crowding and stampedes amplify casualties, highlighting the lethal risks of unmanaged congestion. Kim and Heo [26] developed an agent-based radiological evacuation model that integrates hazard spread with crowd behavior, emphasizing the importance of coupling human movement with evolving risks. Ding et al. [27] proposed a building-information-driven framework linking fire dynamics with crowd simulation, demonstrating how real-time route optimization can mitigate congestion. Other works have focused on strategy optimization: Yang et al. [28] optimized metro-station evacuation routes under potential stampedes, while Lu and Li [29] applied machine learning to improve fire evacuation outcomes by influencing evacuee behavior, such as staggered exits or enhanced risk awareness. Together, these studies illustrate a clear trend toward integrating physical crowd dynamics with technological or operational controls.

Nonetheless, how to intervene by integrating reassurance or by physically guiding movers remains insufficiently quantified. From this, practical control strategies have started to transition from simulation to deployment [9]. Experiments demonstrated that a small obstacle placed just upstream of an exit can smooth inflow and raise outflow [30]. The signage based on reinforcement-learning, updating in real time, was found to steer evacuees around blockages and outperform static guides in virtual-reality tests [31]. Optimization studies further indicated that a few well-positioned human or robotic "evacuation assistants" are able to maximize flows [32]. Finally, a modeling study showed that rapidly broadcasting safety messages and muting hazard rumors suppress panic contagion and stabilize crowd motion [33].

Yet these strategies, while effective in specific settings, often remain fragmented: they target either physical congestion or psychological contagion, but rarely both in an integrated framework. To overcome these limitations, we propose a unified framework that couples contagion dynamics with microscopic motion and allows adaptive interventions to be evaluated systematically across scenarios. Compared with existing studies, our framework provides superior predictive and operational value, as it quantifies intervention effects across diverse layouts and risk regimes and directly links behavioral stabilization to measurable safety outcomes. To address these gaps, this work integrates a weighted small-world contagion field with an extended social force model, introduces adaptive control that selects nodes by combined degree and k-shell ranking, and compares these interventions in a real head-tracking dataset and typical layouts. The results offer quantitative guidelines for balancing physiological and psychological measures in real-time crowd management.

The rest of this paper is organized as follows. Section 2 introduces the modeling framework covering the small-world interaction network, the emotion-contagion mechanism, and the extended social force dynamics augmented with queuing behavior. Section 3 reports a series of numerical studies: (i) natural recovery under varying risk levels, (ii) impact of control measures on phase transitions, and (iii) identification of key nodes in diverse layouts. Section 4 discusses the practical implications, outlines limitations, and future directions.

2. Methods

2.1. Mathematical model

2.1.1. Interaction network

Emergency evacuation involves multilayered interpersonal influences that are both spatial and emotional. To capture this complexity, we construct a dynamic small-world graph [34], where each node represents an individual, and the edge e_{ij} between nodes i and j is formed if either (i) the Euclidean distance d_{ij} falls below a local interaction radius, or (ii) they are connected through a long-range channel such as visual or auditory communication. The link weight C_{ij} of the edge decays with distance, as given by:

$$C_{ij} = \exp\left[-d_{ij}^2/(2\sigma^2)\right] \tag{1}$$

where σ is a scale constant. Moreover, the long-range interaction has a probability $p(t)$ of being reconnected:

$$p(t) = p_0 + \Delta p\, H(t - t_{\text{event}}) \tag{2}$$

Here, p_0 is a baseline probability, and a sudden scream at t_{event} (represented by the step function H) will raise the long-range connectivity by Δp until the panic subsides.

At each time step t, we rebuild $G_t = (V, E_t)$ from the current positions, so that links appear and disappear as pedestrians move (as shown in Fig. 1). Short-range contacts use a distance threshold $r_{\text{prox}} = 1.0\,\text{m}$ and weights $C_{ij}(t) = \exp[-d_{ij}(t)^2/(2\sigma^2)]$ with $\sigma = 1.0\,\text{m}$, while long-range shortcuts created by rewiring are assigned unit weight. Rewiring acts on the short-range edge set and, with probability $p(t)$, replaces an existing endpoint by a uniformly sampled target ($i \neq j$), thereby generating a Watts–Strogatz–style small-world topology without freezing early contacts. In practice, we update the network every $\Delta t_{\text{net}} = 5$ frames (0.20 s), which captures transient encounters and avoids artifacts of a static graph. In our baseline geometry, this construction yields an instantaneous average degree $\langle k \rangle \approx 12$ and clustering coefficient $C \approx 0.30$, consistent with empirical proximity networks. During the panic window defined by $H(t - t_{\text{event}}) = 1$, we set $p(t)$ such that $p_0 = 0.004$ increases to $p(t) \approx 0.20$, while the probability reverts to p_0 outside that window.

2.1.2. Impatience dynamics

Let $\omega_i(t) \in [0, 1]$ denote the impatience of pedestrian i, that is, the tendency to abandon orderly queuing. The socio-psychological evidence shows that ω_i tends to increase if surrounding neighbors misbehave or if the perceived local danger η_i exacerbates [35]. The impatience is therefore updated as follows:

$$\omega_i(t+\Delta t) = \beta\, \omega_i(t) + (1 - \beta)\Big[\alpha\, \overline{\omega}_{N_i}(t) + (1 - \alpha)\, g(\eta_i) \Big] \tag{3}$$

where $\beta \in [0, 1]$ is a time decay factor that controls memory, α is a weighted coefficient that balances social influence and environmental risk, and $g(\eta_i) = \big[1 + \exp(-k_\eta(\eta_i - \eta_0))\big]^{-1}$ is a sigmoid response to risk. Here, N_i is the neighbor set of pedestrian i, and the average impatience of its neighbors is computed as follows:

$$\overline{\omega}_{N_i}(t) = \frac{\sum\limits_{j \in N_i} \omega_j(t)\, C_{ij}}{\sum\limits_{j \in N_i} C_{ij}} \tag{4}$$

2.1.3. Pedestrian movement

The motion equation of pedestrian i is governed by an extended social force model [15,16], in which the temporal variation of velocity $\mathbf{v}_i(t)$ is updated by:

$$m_i \frac{d\mathbf{v}_i(t)}{dt} = \mathbf{f}_i^{\text{self}} + \sum_{j \neq i} \mathbf{f}_{ij} + \sum_W \mathbf{f}_{iW} \tag{5}$$

Here, the self-driven force combines the classical desired-velocity relaxation term with a queuing alignment interaction:

$$\mathbf{f}_i^{\text{self}} = m_i \frac{v_i^0(t)\, \mathbf{e}_i^0(t) - \mathbf{v}_i(t)}{\tau_i} + \mathbf{f}_i^{\text{queue}} \tag{6}$$

where m_i is the pedestrian mass, τ_i is a relaxation time, and the expected direction $\mathbf{e}_i^0$ mixes an optimal direction $\mathbf{e}_i^{des}$ toward the exit [36] and a direction $\hat{\mathbf{d}}_i$ to follow the queue [35] (see Fig. 2):

$$\mathbf{e}_i^0(t + \Delta t) = \frac{\omega_i(t)\, \hat{\mathbf{d}}_i(t + \Delta t) + [1 - \omega_i(t)]\, \mathbf{e}_i^{des}}{\big\| \omega_i(t)\, \hat{\mathbf{d}}_i(t + \Delta t) + [1 - \omega_i(t)]\, \mathbf{e}_i^{des} \big\|} \tag{7}$$

In addition, the expected speed follows the heuristic rule $v_i^0(t) = \min\big(d_{ij}/\tau_i,\ v_i^{init}\big)$, where v_i^{init} is the initial desired speed of pedestrian i, which encourages deceleration when close to another pedestrian j ahead. Based on empirical findings, the queued pedestrians align
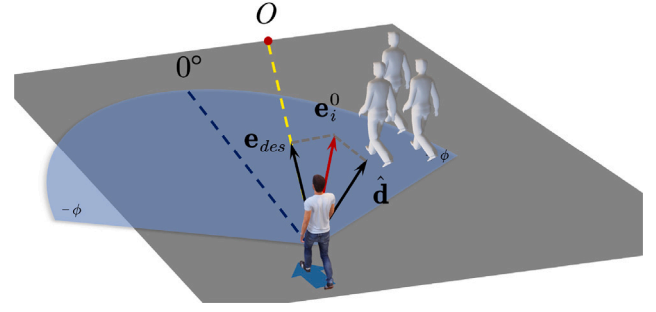

Fig. 2. Schematic of pedestrian movement. The focal pedestrian (highlighted) makes a trade-off between the collective flow direction of nearby neighbors and the direct direction toward the exit.

Table 1
Contagion and network parameters.

Symbol	Description	Value
r_{prox}	Proximity radius (short range)	1.0 m
σ	Distance-decay scale	1.0 m
p_0	Baseline rewiring probability	0.004
p_{panic}	Rewiring under panic window	0.20
Δt_{net}	Network rebuild cadence	0.20 s (5 frames)
α	Social vs. risk weighting	0.5
β	Memory/decay factor	0.8
η	Pressure-induced increment	0.02
f_c	Contact threshold for pressure coupling	40 N

Table 2
Social force, geometry, and numerical settings.

Symbol	Description	Value
μ_v, σ_v	Free-speed distribution	$1.30 \pm 0.30\,\text{m s}^{-1}$
m_i	Pedestrian mass	80 kg
r_i	Body radius	0.15~0.20 m
τ_i	Relaxation time	0.5 s
A_i	Social repulsion constant	$5 \times 10^2\,\text{kg m s}^{-2}$
B_i	Range of social repulsion	0.08 m
k	Body elasticity	$1.2 \times 10^5\,\text{kg s}^{-2}$
κ	Sliding friction	$2.4 \times 10^5\,\text{kg m}^{-1}\,\text{s}^{-1}$
c	Queue-alignment gain	$5 \times 10^3\,\text{kg m}^{-1}\,\text{s}^{-2}$
Δt	Simulation time step	0.04 s

laterally along a line perpendicular to the center of the exit. As a result, a queue-forming force is expressed as below:

$$\mathbf{f}_i^{\text{queue}} = c\, \omega_i(t)\, (x_i - x_0)\, \mathbf{e}_x, \tag{8}$$

where c represents a scaling factor, x_i and x_0 respectively denote the horizontal position of pedestrian i and the center of the exit, and $\mathbf{e}_x$ points laterally.

The two interaction forces with other individuals and the wall are written as:

$$\mathbf{f}_{ij} = \Big[A_i\, e^{(r_{ij} - d_{ij})/B_i} + k\, g(r_{ij} - d_{ij})\Big]\mathbf{n}_{ij} + \kappa\, g(r_{ij} - d_{ij})\, \Delta v_{ij}^t\, \mathbf{t}_{ij} \tag{9}$$

$$\mathbf{f}_{iW} = \Big[A_i\, e^{(r_i - d_{iW})/B_i} + k\, g(r_i - d_{iW})\Big]\mathbf{n}_{iW} - \kappa\, g(r_i - d_{iW})\, (\mathbf{v}_i \cdot \mathbf{t}_{iW})\, \mathbf{t}_{iW} \tag{10}$$

For further aspects regarding the parameters in the above equations, see Ref. [16].

To ensure direct comparability, as shown in Tables 1 and 2, all parameter values follow prior evacuation studies [15,36]. Parts of the background description of the social force interactions and the alignment metric are paraphrased and extended from our earlier report in Yi et al. [35]; we refer readers there for complementary experimental details and retain all new control-related elements herein.

2.1.4. Pressure-induced emotion amplification

High-density crowding is a central practical challenge in evacuation safety, as it often gives rise to life-threatening hazards such as clogging, surging, and even crowd crush disasters. Understanding the mechanisms by which congestion forms and amplifies is therefore essential to ensure that any proposed control framework can be applied in realistic scenarios. In this section, we highlight the key physical and psychological processes that characterize dense-crowd phenomena and explain why they must be explicitly considered when designing interventions. In particular, when density exceeds a critical threshold, even small perturbations can trigger turbulent motion and arching at exits [37], while physical pressure and close contact can rapidly escalate into panic through emotional contagion. This interplay between mechanical forces and psychological stress explains the abrupt breakdown of order that is frequently observed in crowd disasters. Extensive field observations show that strong pushing or bodily contact in dense crowds can precipitate a sudden surge of anxiety or panic [16,36]. Whereas the contagion model in Section 2.1.2 captures social routes of emotion propagation, it does not account for this physical trigger. We therefore augment the impatience dynamics with a pressure-triggered term that couples local contact forces to psychological stress.

Let $\omega_i(t) \in [0, 1]$ denote the impatience level of pedestrian i at time t. After the contagion update $\Delta\omega_i^{\text{contagion}}$ has been computed (Eq. (3)), the final update is

$$\omega_i(t + \Delta t) = \omega_i(t) + \Delta\omega_i^{\text{contagion}} + \Delta\omega_i^{\text{pressure}}, \tag{11}$$

Here, the pressure-induced increment $\Delta\omega_i^{\text{pressure}} = \eta \, \mathbb{1}(f_i^{\text{contact}} > f_c)$ is defined by the step function, where $\mathbb{1}(\cdot)$ is the indicator function and $f_i^{\text{contact}} = \sum_{j \in \mathcal{N}_i} \|f_{ij}^{\text{repulsion}}\|$. We use $\mathbf{f}_{ij}^{\text{repulsion}}$ to denote only the exponential social-repulsion term in Eq. (9), and f_i^{contact} is the total pushing force that pedestrian i experiences from its neighbors during the current step.

Laboratory and simulation studies report that noticeable psychological stress is triggered when local pushing forces exceed roughly 30–50 N [16,36]. Recent density–emotion models introduce a comparable threshold and an amplification parameter to reproduce panic surges [38]. Guided by these findings, we set the default values (see Table 1) to $f_c = 40$ N and $\eta = 0.02$, so that a single strong shove produces an emotion increment comparable to a typical contagion step. These considerations indicate that dense-crowd hazards are not merely theoretical, but arise from the tight coupling of physical forces and emotional contagion. Our framework builds on this understanding by explicitly introducing a pressure-triggered component into the impatience dynamics, and by evaluating how topology-aware interventions can suppress the feedback loop between stress and congestion. This coupling yields a multi-scale interaction: physical forces operate in the lower (movement) layer, while their exceedance of the perceptual threshold instantly feeds into the upper (emotional) layer, enabling the model to reproduce abrupt breakdowns of order that occur in high-density crowds.

2.2. Control measures and network node analysis

Integrating positive-emotion contagion mechanisms into the crowd evacuation model is well motivated by psychological and coordination considerations. Existing studies have denoted that positive affect predisposes individuals to prosocial and cooperative behaviors [39,40]. For example, interventions that enhance feelings of joy or gratitude lead people to act more friendly toward others. The positive emotions play a stabilizing role in agent-based evacuation models; that is, agents with positive emotions are more likely to synchronize and self-organize. Therefore, introducing explicit positive-emotion dynamics is reasonable and necessary because it allows agents to resist panic and propagate calming effects across the crowd, which ultimately assists in promoting order and cooperation during evacuation.
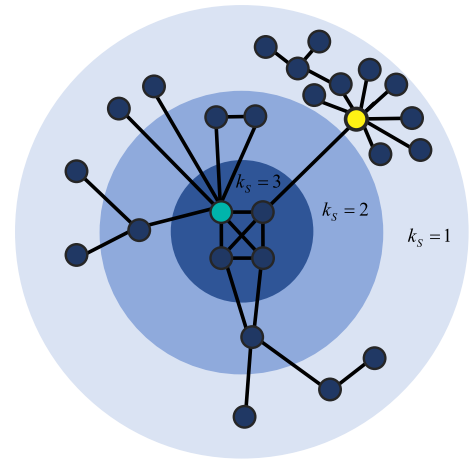

Fig. 3. Illustration of k-shell decomposition. Although cyan and yellow nodes each have degree $k = 8$, their roles differ markedly: the yellow node resides on the network's periphery ($k_s = 1$), whereas the cyan node is a core hub with the maximum shell index ($k_s = 3$).

To identify key nodes for intervention, we adopt two widely used centrality measures: degree centrality and k-shell index. The degree centrality quantifies the number of direct connections a node has, and nodes with high degrees often act as local hubs that influence many agents. In contrast, the k-shell (or k-core) decomposition [41] partitions the network into nested shells by iteratively removing nodes with degree less than k to reveal the hierarchical structure [42]. The k-shell index of a node indicates the deepest shell it belongs to. While high degree nodes exert strong local influence, high k-shell nodes are structurally embedded in the network core and tend to have more widespread impact. A schematic in Fig. 3 illustrates this distinction: two nodes may share the same degrees but differ significantly in their k-shell values, reflecting their different roles in network connectivity.

We consider two types of intervention mechanisms targeted at key nodes. The first is positive-emotion injection, aiming to directly reduce the emotional arousal of selected pedestrians. Let the impatience $\omega_i(t)$ of pedestrian i represent its emotional state, which can be updated under this intervention as follows:

$$\omega_i(t + \Delta t) = \omega_i(t) - \gamma \cdot \mathbf{1}_{[t_0, t_0+T]}(t) \tag{12}$$

Here, γ is the intervention intensity, and $\mathbf{1}_{[t_0, t_0+T]}$ is the indicator function for the intervention period, where t_0 and T are initial time and duration, respectively. This models real-world calming strategies, such as targeted audio or visual messages.

The intervention proceeds in the following order: (i) apply the emotion pulse by the update above, (ii) compute the neighborhood term using a masked emission, and (iii) perform the contagion update for all agents using the standard rule with $\omega_{\mathcal{N}_i}(t)$ (and α, β as specified elsewhere). In other words, controlled agents receive a positive-emotion pulse that lowers their own ω_i and emit no panic to neighbors during the intervention window, thus they still receive social influence from others.

The second mechanism is directional guidance, which represents a tendency to steer individuals toward queuing behavior or coordinated motion. Let $\mathbf{g}_i$ denote the guiding direction (e.g., along a queue), then a guiding force is defined as:

$$\mathbf{f}_i^{\text{guide}} = \lambda \cdot \mathbf{g}_i \tag{13}$$

where λ is the strength of the guidance, whose value can be made adaptive, increasing in response to local density or crowd conditions. This force encourages alignment with the desired flow, which enhances orderliness and mitigates lateral conflicts. Overall, these mechanisms
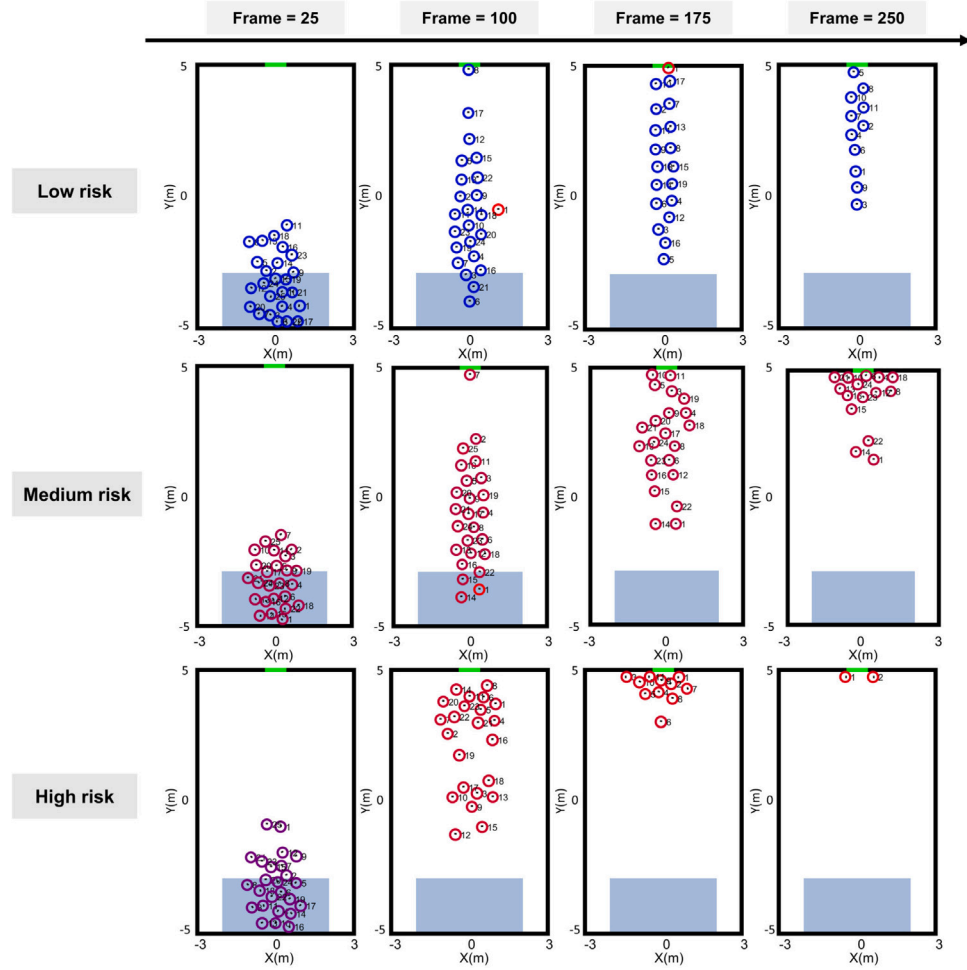
Fig. 4. Typical snapshots of crowd evacuation under the three risk levels. The solid black lines indicate the building geometry, the green strip marks the exit, and the light blue area denotes the initial pedestrian distribution. Each circle represents a pedestrian, whose color encodes the emotional state, with blue and red indicating calm and panic states, respectively.

provide interpretable and adjustable control strategies that influence both the physiological and psychological aspects of pedestrian behavior, thereby making it possible to study order formation under targeted interventions.

3. Numerical experiments

3.1. Natural recovery from disorder

The coupling between the emotion-propagation network and the extended social force model has been quantitatively validated in our previous research [43]. Therefore, we omit further calibration in this work and focus directly on intervention strategy exploration. We simulate the post-shock recovery dynamics of pedestrian crowds under the three risk levels (i.e., low, medium, and high), which are distinguished by modest changes in environmental cues (e.g., noise level, visual danger signals). These risk settings, primarily used to modulate the initial emotional states of individuals, are briefly described here because our interest lies in the dynamical characteristics after the panic event. In each scenario, we model a crowd of $N = 25$ pedestrians as an initial size, and subsequent sections repeat the analysis for larger N to assess robustness. At time frame 80, a sudden shouting event is introduced to represent an abrupt panic trigger. The long-range interaction probability in the emotional contagion network is increased to $p(t) = 0.2$ (from its lower baseline value) to simulate the spread of intensified panic. After time frame 100, this probability $p(t)$ reverts
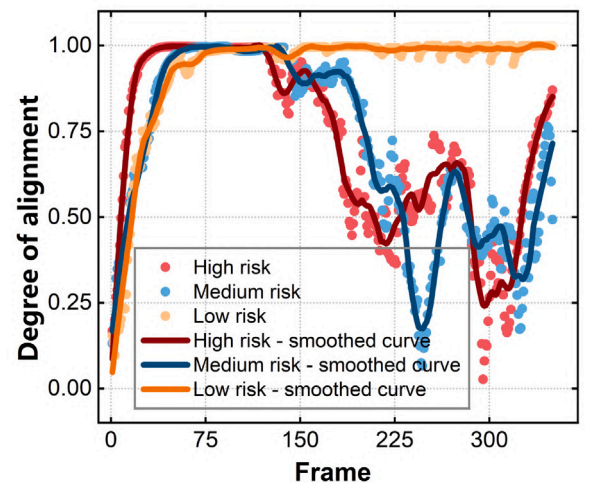
Fig. 5. Temporal evolutions of alignment under the three risk levels. The solid curves display the smoothed trajectories derived from the raw time-series data.

to its baseline value $p_0 = 0.004$. The emotional contagion mechanism follows recent models in which adding emotional interactions enhances behavioral realism in stressful situations.
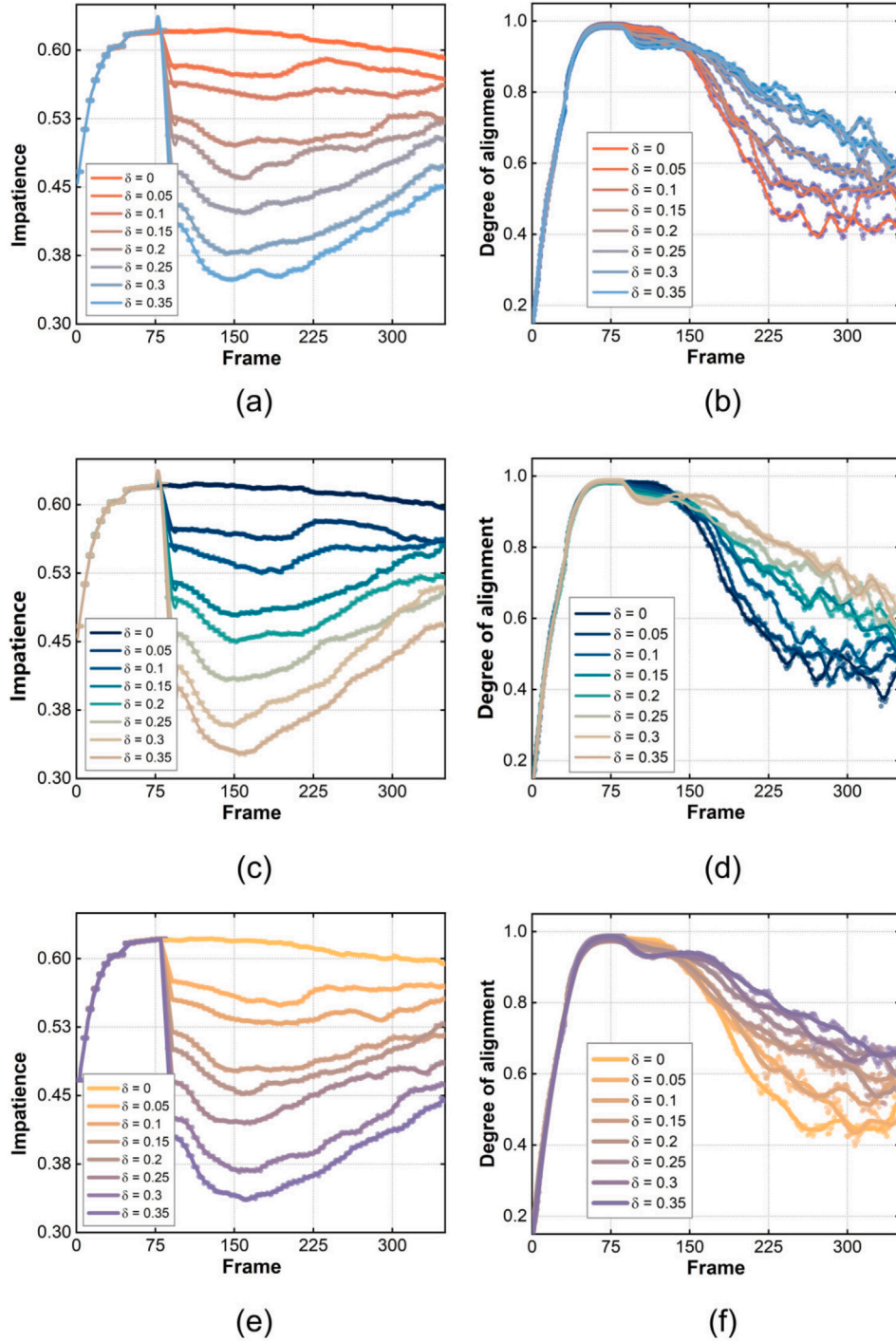
Fig. 6. Temporal evolutions of impatience and alignment under different intervention strategies. (a)–(b) Targeting random nodes. (c)–(d) Targeting high degree nodes. (e)–(f) Targeting high k–shell nodes.

We quantify collective order using an alignment metric $A(t)$, which is defined as the mean cosine similarity of all pairwise pedestrian velocity directions:

$$A(t) = \frac{2}{N(N-1)} \sum_{i<j} \hat{\mathbf{v}}_i(t) \cdot \hat{\mathbf{v}}_j(t), \tag{14}$$

where $\hat{\mathbf{v}}_i(t) = \mathbf{v}_i(t)/|\mathbf{v}_i(t)|$ is the unit velocity vector of pedestrian i. Here, $A(t) = 1$ reflects perfect alignment, while $A(t) = 0$ corresponds to complete directional randomness. We record $A(t)$ and the emotional state of each agent throughout each run. Fig. 4 shows typical snapshots of crowd evacuation under the three risk levels (agents colored by

emotional state), and the temporal evolutions of alignment for these cases are presented in Fig. 5.

Under the low risk condition, the crowd rapidly rebuilds order after the disruption. In these runs, $A(t)$ experiences only a brief drop at the shock and then quickly returns to near its pre-shock value. For example, Fig. 4 displays that the agents have largely realigned into a coherent flow by time frame 100, and Fig. 5 confirms that $A(t)$ rebounds to near unity. By contrast, the medium risk scenario exhibits near-critical behavior in which the shock induces a sudden collapse in alignment. As shown in Fig. 5, $A(t)$ decreases sharply after the disturbance and remains low for the rest of the simulation, indicating a rapid transition
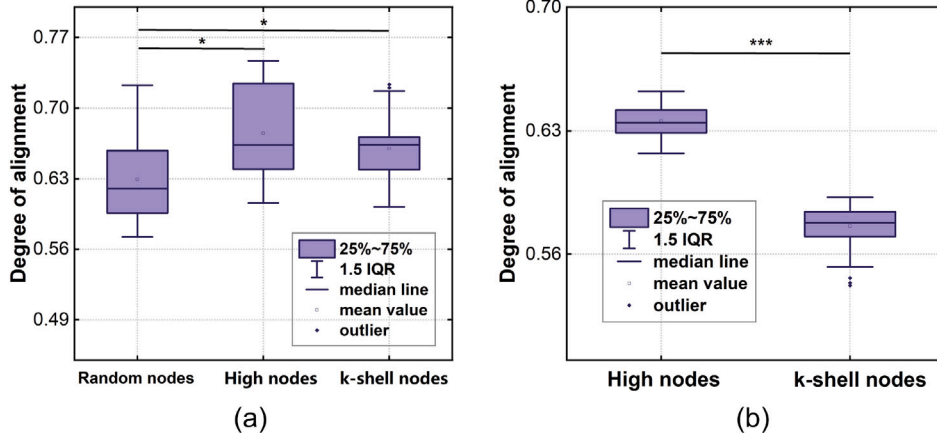
Fig. 7. Quantitative comparison of control effectiveness under different intervention strategies. (a) A crowd of $N = 25$ pedestrians. (b) A crowd of $N = 45$ pedestrians.
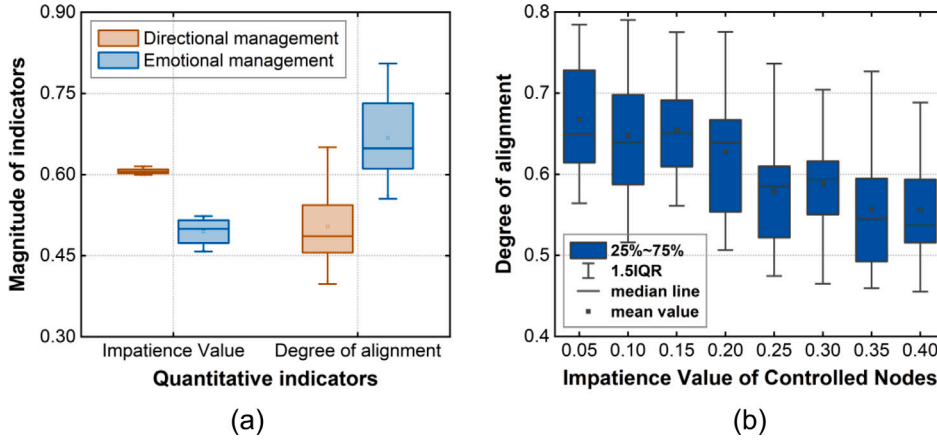

Fig. 8. Quantitative comparison of evacuation indicators. (a) Impatience and alignment under directional and emotional managements. (b) Alignment under varying impatience after emotional management.

from ordered motion to a disordered panic state. This abrupt loss of coherence is analogous to a discontinuous (first-order) phase transition from order to disorder, as reported in collective motion models. That is, in the medium-risk case, the crowd crosses a critical threshold at the moment of shock, beyond which disorder does not naturally return to order even after the perturbation is removed. Finally, the system remains disordered throughout the high-risk simulation. The alignment $A(t)$ even falls close to zero after the shock (Fig. 5) and agents persist in a chaotic configuration (Fig. 4), which suggests that a high baseline threat can prevent spontaneous recovery. In summary, we find that low risk allows natural recovery of collective order after a panic event, but medium risk places the system at a critical point with a phase transition-like collapse, and high risk results in persistent disorder.

3.2. Impact of control measures on phase transitions

3.2.1. Coverage and strategy comparison

In this section, we investigate how external control measures re-shape this transition. We consider three intervention strategies for selecting a fraction δ of specific nodes: (i) targeting random nodes, (ii) targeting high degree nodes, and (iii) targeting high k–shell nodes. Fig. 6 presents the temporal evolutions of impatience and alignment under different intervention strategies. For the case of random-based strategy, as shown in Fig. 6(a)–(b), the post-shock time series of impatience decreases monotonically as δ increases, and the rebound becomes delayed. The divergence in alignment trajectories emerges almost after
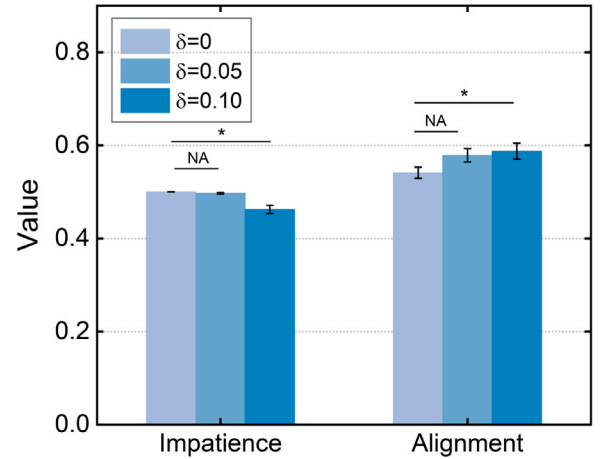

Fig. 9. Low-coverage effectiveness. Mean±SEM ($n = 30$) for impatience and alignment at $\delta \in \{0, 0.05, 0.10\}$. $\delta = 0.10$ reduces impatience and increases alignment; $\delta = 0.05$ is not significant (NA) vs. baseline.

time frame 75, and the following decay rate of alignment falls from approximately 3×10^{-3} frame^{-1} at $\delta = 0$ to 1×10^{-3} frame^{-1} at $\delta = 0.35$. Notably, these curves almost overlap once $\delta \geq 0.25$, indicating it reaches saturation beyond roughly one-fourth coverage. In contrast,
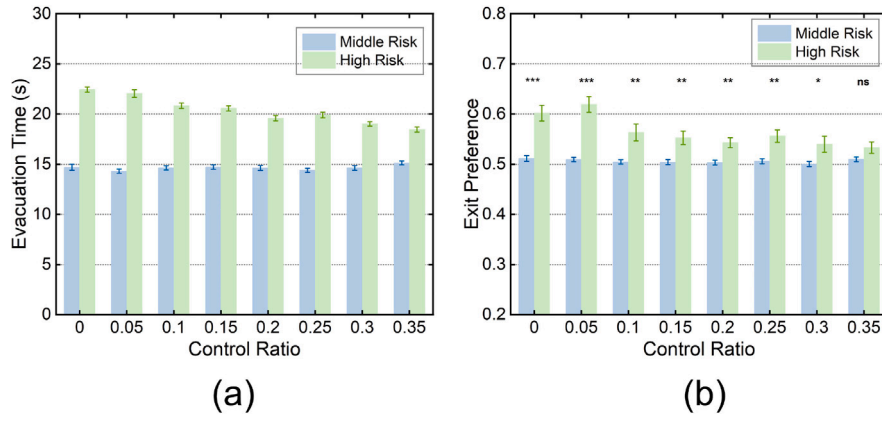
Fig. 10. Dual-exit performance under risk. (a) Evacuation time T (s) versus control ratio δ for middle vs. high risk. With random-walk disorientation and pressure–emotion coupling active, T decreases with δ at high risk, while changes at middle risk are small. (b) Exit preference R_1 (0.5 indicates balanced use of the two exits) versus δ; increasing δ drives $R_1 \to 0.5$ at high risk (significance marks above bars; ns = not significant). Bars show mean±SEM ($n = 30$; multiple-comparison corrected).
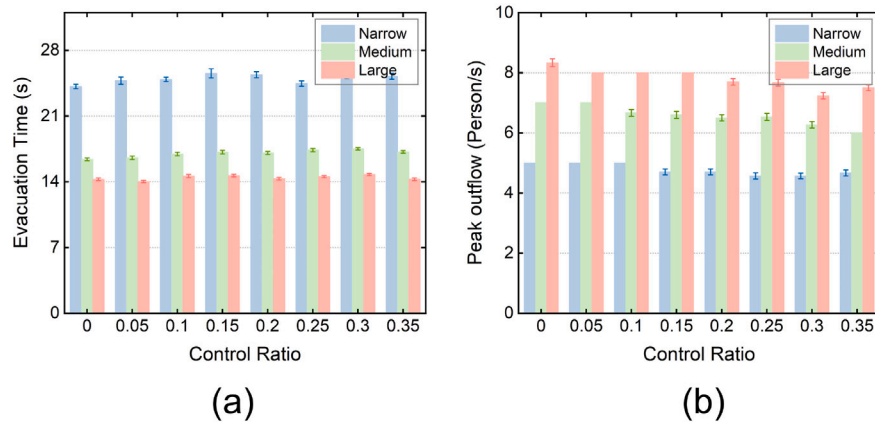
Fig. 11. Exit-width sweep. (a) Evacuation time T (s) versus control ratio δ for narrow/medium/large doors. At saturated narrow doors, T changes little (capacity-limited), whereas wider doors show modest decreases as δ increases. (b) Peak out-flow (persons/s) versus δ; control slightly reduces peakiness at narrow doors and maintains high outflow at wider doors. Bars show mean±SEM ($n = 30$).

degree-based and k-shell-based strategies produce significantly stronger effects in Fig. 6(c)–(f). For instance, at time frame 200, the mean impatience is roughly 16% lower and the mean alignment about 12% higher than those achieved by the random-based strategy at the same δ. Although the absolute performance of these two strategies is comparable, the k-shell-based strategy exhibits a lower run-to-run fluctuation, suggesting that it has slightly greater robustness.

Previous theoretical and empirical studies have reported that influencing 10%–20% of nodes is sufficient to change the behavior of global networks [44]. From this, we focus on the case of $\delta = 0.2$ (saturation after $\delta = 0.25$) and compare the control effectiveness under different intervention strategies. At a relatively low density ($N = 25$), as shown in Fig. 7(a), both targeted strategies significantly outperform random-based strategy (p-value < 0.01), and the pairwise Mann–Whitney tests show that the median gains are $\Delta A \approx 0.05$ for degree-based and $\Delta A \approx 0.04$ for k-shell-based strategies, while the difference between them is not statistically significant. As density increases ($N = 45$), Fig. 7(b) illustrates that degree-based strategy retains roughly 70% of its original benefit, whereas the effectiveness of k-shell-based strategy declines to about 40%. This reveals that the degree-based strategy is more beneficial for scaling with density, even though k-shell nodes may remain attractive in situations requiring rapid and cohesive influence. It should be noted that a clear inflection point at $\delta \in [0.15, 0.2]$ can be found by integrating the alignment curves over time, where additional coverage beyond this range yields an increment of less than 5%.

Further, the quantitative comparison of evacuation indicators is presented in Fig. 8. For the same targeted nodes, Fig. 8(a) reveals emotional management shows better control effects than directional management in terms of both impatience and alignment. Fig. 8(b) shows the alignment under varying impatience after emotional management: all control levels perform similarly if $\omega \leq 0.2$, but the alignment collapses toward the non-control level if $\omega \geq 0.25$. Thus, we can reduce impatience to below this threshold using effective management, with emotional guidance achieving this more efficiently. Overall, our simulations show that applying positive-emotion pulses to about 20% of strategically chosen pedestrians (preferably high degree or high k-shell nodes at lower densities) can suppress the order–disorder phase transition, reduce impatience peaks, and preserve high directional coherence. This offers a practical guideline for crowd management protocols in emergency situations.

3.2.2. Low-coverage effectiveness

A practical question is whether small but realistic coverage remains beneficial. Fig. 9 shows that even $\delta = 0.10$ produces statistically significant improvements over the baseline ($p < 0.05$), whereas $\delta =$
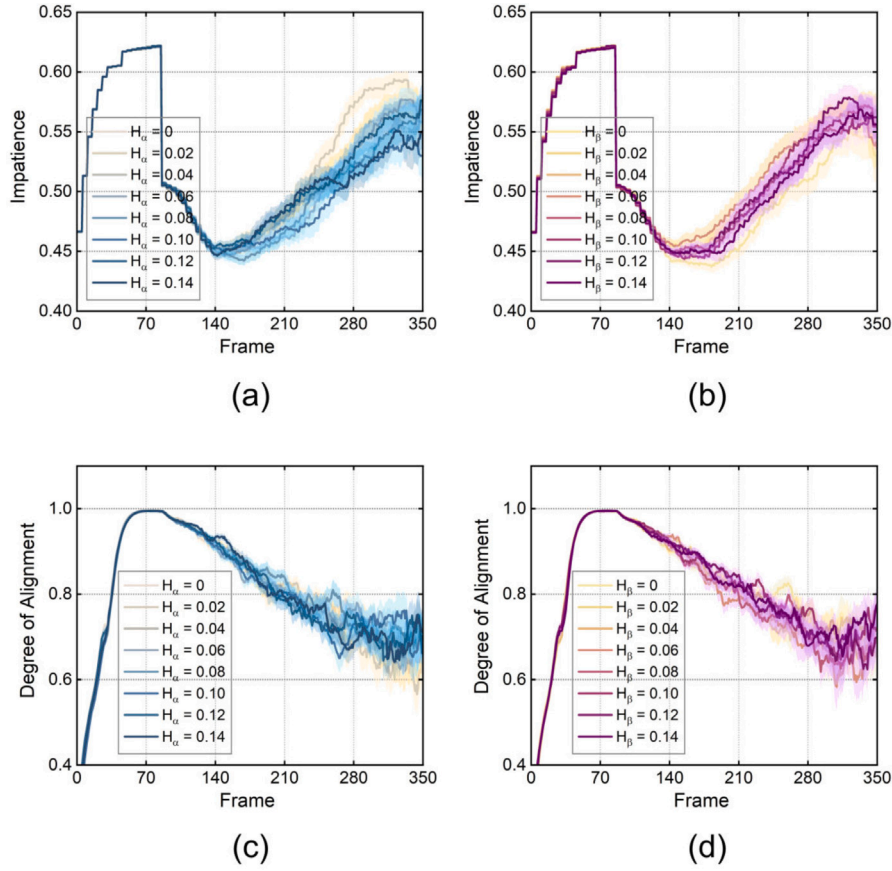
Fig. 12. Individual heterogeneity. Time series of impatience (a,b) and alignment (c,d) under increasing heterogeneity in the social–risk weighting (H_α, left column) and the memory/decay factor (H_β, right column). Solid lines show the mean with shaded SEM ($n = 30$).

0.05 is generally indistinguishable from no control ($p > 0.10$). Gains grow sublinearly with δ, suggesting 10–15% as a feasible target range via hybrid deployments (mobile stewards plus targeted signage), while 20% can be viewed as an upper-bound stress test.

3.2.3. Dual-exit performance under high risk

Dual-exit layouts introduce additional coordination demands because misperception can amplify exit imbalance. In this setting, we activate two mechanisms as follows. (i) Random-walk disorientation rule: when impatience exceeds a threshold, temporarily replaces the desired direction with a random unit vector for a short random duration. (ii) Pressure–emotion coupling: excessive local contact force raises impatience via a thresholded increment. With these mechanisms, topology-aware control that raises alignment (HD or HK at $\delta \in [0.15, 0.20]$) shortens the total evacuation time T by $\approx 12\%$, reduces the exit-preference bias R_1 by $\approx 23\%$ toward balanced usage, and lowers the peak contact force (all $p < 0.01$, $n = 30$, BH–FDR). The improvement arises because influential nodes recover from disorientation earlier and dampen rumor-like spread of erratic headings, curtailing the positive feedback between confusion and compression. The effects on T are small at medium risk, consistent with already stable dynamics (Fig. 10).

3.2.4. Robustness to parameter heterogeneity

We next assess robustness of the intervention effects across three dimensions: (i) geometry via exit-width variation, (ii) social reach via the long-range contagion probability $p(t)$, and (iii) individual variability via moderate parameter heterogeneity. Throughout we keep the statistical protocol unchanged (mean±SEM, $n = 30$, BH–FDR).

Exit-width sweep (geometry). Across narrow, medium, and wide single-exit layouts (Fig. 11), both HD and HK consistently reduce impatience peaks and raise alignment relative to random or no control. Operationally, at a saturated narrow door the total evacuation time T is capacity-limited and thus shows at most marginal reductions (or a negligible increase consistent with a stability–outflow trade-off), yet peak contact force is lowered and 1 s peak outflow is smoothed. As the door widens and the bottleneck constraint relaxes, modest decreases in T emerge while the safety-related gains (lower peak force, higher alignment) persist. These patterns indicate that topology-aware control mainly improves stability and safety under strict capacity, and additionally shortens T when geometry ceases to be the dominant limiter.

Long-range contagion sweep (social reach). We varied the baseline long-range probability p_0 from 0 to 0.006 at medium density while holding the panic-window amplitude fixed. In all cases, targeted control (HD and HK) delayed the alignment collapse and reduced residual impatience relative to no control. Comparing HD with HK, the alignment advantage of HD was consistently but only slightly larger across the tested p_0 values, and the differences did not reach statistical significance under nonparametric tests. Thus, within this p_0 range, the two strategies can be regarded as broadly comparable, with a mild practical edge for HD as social reach strengthens. The coverage–benefit "elbow" remains near $\delta \in [0.15, 0.20]$, beyond which returns diminish.

Individual heterogeneity (parameters). Free speeds are sampled from $\mathcal{N}(1.30, 0.30^2)$ m/s, and per-agent (α_i, β_i) are drawn as bounded perturbations around global means to induce moderate heterogeneity.
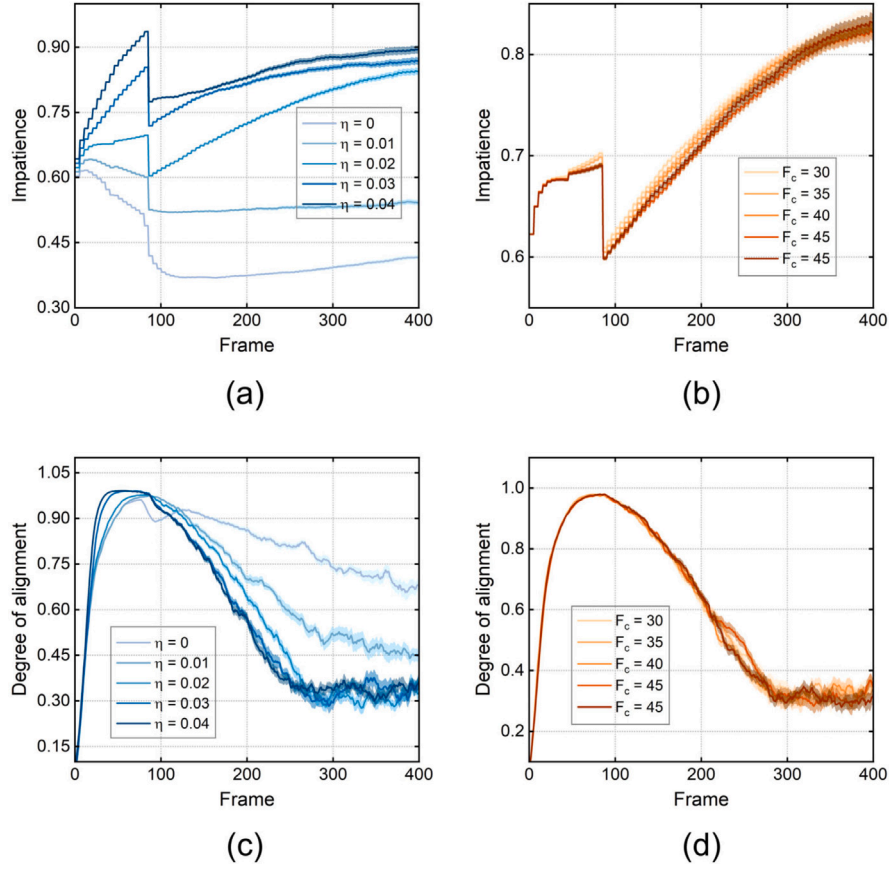
Fig. 13. Sensitivity to pressure–emotion coupling. Impatience (a,b) and alignment (c,d) under sweeps of amplification η (left) and threshold f_c (right). Larger η and lower f_c intensify and prolong pressure-triggered impatience and erode alignment; the baseline ($f_c = 40\,\text{N}$, $\eta = 0.02$) is mid-range.

Sensitivity sweeps show that increasing heterogeneity broadens dispersion and slightly delays recovery. However, the qualitative ranking between HD and HK — and their gains at $\delta \in \{0.10, 0.20\}$ — remains unchanged (Fig. 12). Together with the geometry and $p(t)$ sweeps, these results indicate that the principal conclusions are robust: topology-aware control reliably stabilizes dynamics across layouts and social-reach regimes, improves safety metrics under tight capacity, and preserves its comparative ordering under reasonable inter-individual variability.

3.2.5. High-density validation

In a dense regime (e.g., $N = 70$ in an area of $13.4\,\text{m}^2$, density $5.2\,\text{ped/m}^2$), contacts are transient and force chains frequent. We therefore enable the pressure–emotion coupling and examine (i) the sensitivity to collision-induced parameters and (ii) the effectiveness of control strategies under high density.

Sensitivity to pressure–emotion coupling. Varying amplifications η and contact thresholds f_c show consistent monotone trends: larger η produces higher and more persistent impatience and a faster loss of alignment, whereas lower f_c (easier triggering) yields more frequent pressure-induced increments with similar consequences. The baseline ($f_c = 40\,\text{N}$, $\eta = 0.02$) lies mid-range and is used in the main experiments (Fig. 13).

Effectiveness of strategies at high density. With the coupling active, periodically retargeted high-degree (HD) targeting lowers mean impatience and increases alignment (AUC) relative to no control, k-shell (HK) exhibits the same direction with smaller gains. Both targeted schemes reduce peak contact forces compared to random selection, while the

total evacuation time T changes little or can be slightly longer at saturated doors, which reflects a stability–outflow trade-off typical of capacity-limited bottlenecks (Fig. 14).

3.3. Identification of key nodes in the real world

This section is concerned with identifying key nodes in the real world. We first analyze high-resolution crowd recordings to determine influential individuals. Based on public head-detection datasets [45], the time-resolved interaction networks are constructed, where pedestrians are treated as nodes and proximity-based links are represented as network edges. Over sliding time windows, we extract the sets of the top 20% of high degree (THD) and high k-shell (THK) nodes at each time frame to assess where such structurally "influential" agents actually occur and how stable these selections remain over time.

Fig. 15 shows the spatial distribution of key nodes during evacuation experiments, in which the locations of THD nodes in the early and late stages are mapped in Fig. 15(a)–(b), while the corresponding THK nodes are presented in Fig. 15(c)–(d). It is found that the two sets occupy different regions: THD nodes tend to cluster in the dense core (e.g., bottlenecks or exits) of the crowd, whereas THK nodes are often located at the periphery. This implies that degree centrality highlights locally well-connected individuals, while k-shell centrality captures those deeply embedded in the global contact structure. That is, some agents have many direct contacts but may not lie on the most central network paths, and vice versa.

The temporal evolutions of key-node metrics (i.e., maximum node degree and maximum k-shell index) are shown in Fig. 16. Both curves rise sharply during the initial rush toward the exit, and then decline
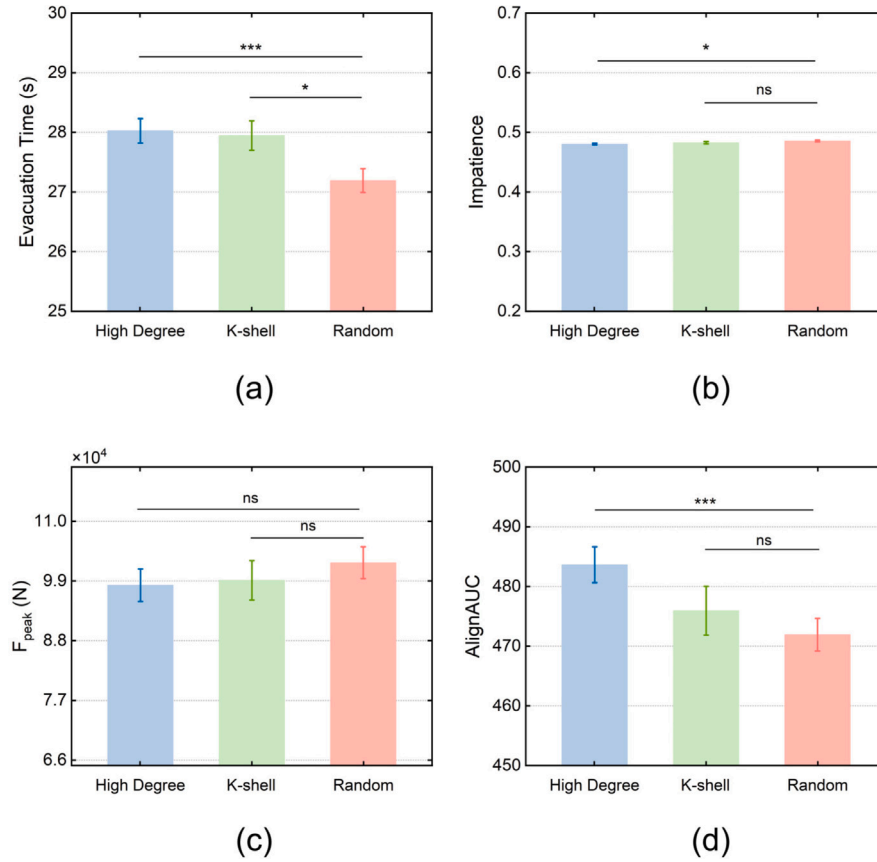
Fig. 14. Strategy effectiveness at high density. (a) Evacuation time T (s), (b) mean impatience, (c) peak contact force F_{peak} (N), and (d) alignment area-under-curve (AlignAUC) for HD, HK, and random control. HD achieves lower impatience and higher AlignAUC than random; HK shows similar but smaller improvements. Both targeted schemes reduce F_{peak} relative to random, while T changes little or may be slightly longer at saturated doors (mean±SEM, $n = 30$).

as the evacuation progresses. This dynamic trend confirms that the identification and importance of key nodes change over time, because a static choice of key nodes will quickly become outdated, which aligns with studies on dynamic networks that emphasize the need to re-evaluate node importance as conditions evolve.

To quantify how different the two criteria are in practice, we computed the Jaccard overlap $J(\delta)$ between the top-δ THD and THK sets on sliding windows across 40 real sequences. Across 40 real sequences, the Jaccard overlap $J(\delta)$ between the top-δ THD and THK sets increases with coverage but remains partial: $\overline{J}(0.10) \approx 0.17$, $\overline{J}(0.15) \approx 0.26$, and $\overline{J}(0.20) \approx 0.32$ (SEM ~ 0.03–0.05). In practice, this supports hybrid policies (e.g., THD ∪ THK) with short retargeting windows to maintain coverage of both dense cores and structural bridges as the contact graph evolves.

To better visualize global spatial patterns, Fig. 17 shows spatial distributions of key-node locations during evacuation experiments, with red regions denoting areas where key nodes appear most frequently. The red area in Fig. 17(a) confirms that THD nodes cluster in the core region of the crowd, whereas Fig. 17(b) reveals that THK nodes are distributed along the outer shell. In practice, this suggests that intervention strategies should consider not only the highest density areas but also the network "bridges" at the edges of dense crowds. To further isolate the effect of spatial geometry on key-node locations, we conduct simulations in four typical architecture layouts: a circular plaza, a T-shaped intersection, a region with internal obstacles, and a semicircular gathering space. As shown in Fig. 18, the contact networks are constructed, and both THD and THK nodes can be identified. In addition, we define a high-density zone ρ as the subset of the region

Table 3
Statistical analysis for different architecture layouts.

| Layout	$\langle d \rangle$	$\langle ks \rangle$	$J(\text{THD, THK})$	$J(\rho, \text{THD})$	$J(\rho, \text{THK})$	$J(\rho \cup \text{Seed, THK})$
Circle	2.41	1.65	0.610	0.359	0.364	0.449
T-cross	2.41	1.65	0.614	0.366	0.371	0.453
Obstacles	3.68	2.40	0.561	0.366	0.375	0.462
Semicircle	2.41	1.65	0.615	0.362	0.371	0.450

containing the top 20% of local density [36]. These architecture layouts are compared in Table 3 using the following statistics: (i) average degree $\langle d \rangle$ of the chosen nodes, (ii) average k-shell $\langle ks \rangle$ of the chosen nodes, and (iii) Jaccard similarity index $J(A, B) = |A \cap B|/|A \cup B|$ between sets A and B. In open layouts (circle, T-shape, semicircle), $\langle d \rangle \approx 2.41$ and $\langle ks \rangle \approx 1.65$ reflect relatively sparse connections, while in the scenario with obstacles, $\langle d \rangle \approx 3.68$ and $\langle ks \rangle \approx 2.40$ exhibit higher connectivity due to the formation of narrow passages. The overlap between degree-based and k–shell–based sets is partial since $J(\text{THD, THK}) \approx 0.61$ in open layouts and $J(\text{THD, THK}) \approx 0.56$ in the obstacle case. Importantly, the overlap between high-density regions and structural key nodes is much lower, with only about one-third ($J(\rho, \text{THD}) \approx 0.36$ and $J(\rho, \text{THK}) \approx 0.38$) of central nodes falling within the top 20% density zone. Even after including the locations of sudden seed events (i.e., long-range panic sources), the overlap with THD or THK nodes only rises to about 0.45.

In summary, our simulations demonstrate that neither local density nor static network topology is sufficient to identify all key nodes. Although high-density areas contain many important individuals, a
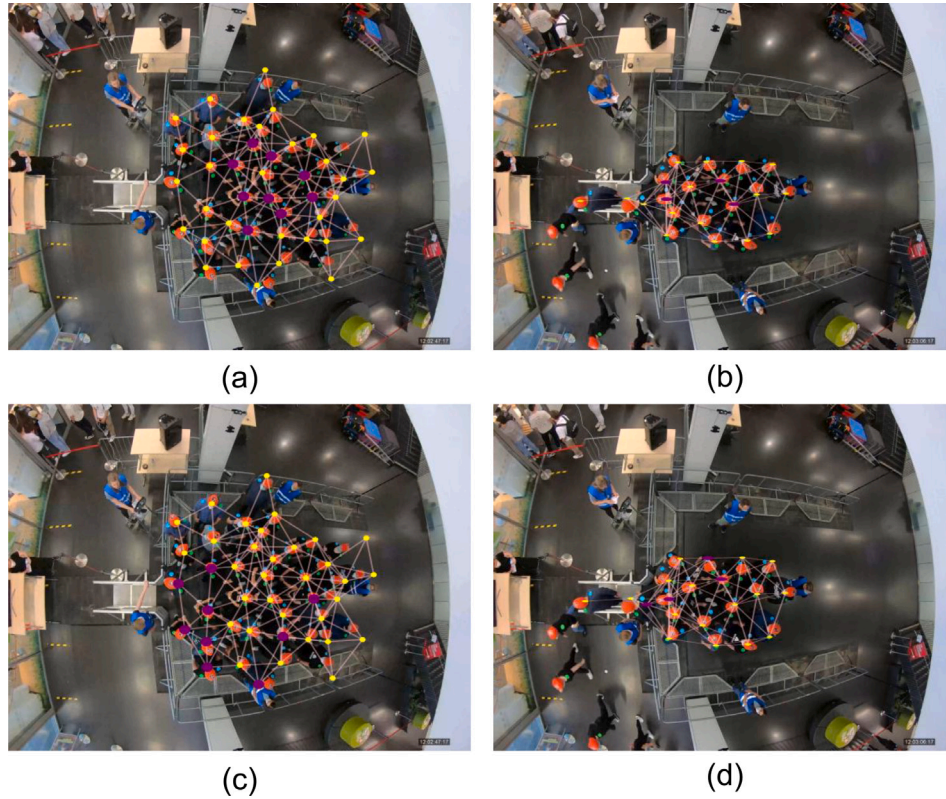
Fig. 15. Locations of key nodes during evacuation experiments. (a)–(b) Locations of THD nodes in the early and late stages. (c)–(d) Locations of THK nodes in the early and late stages.
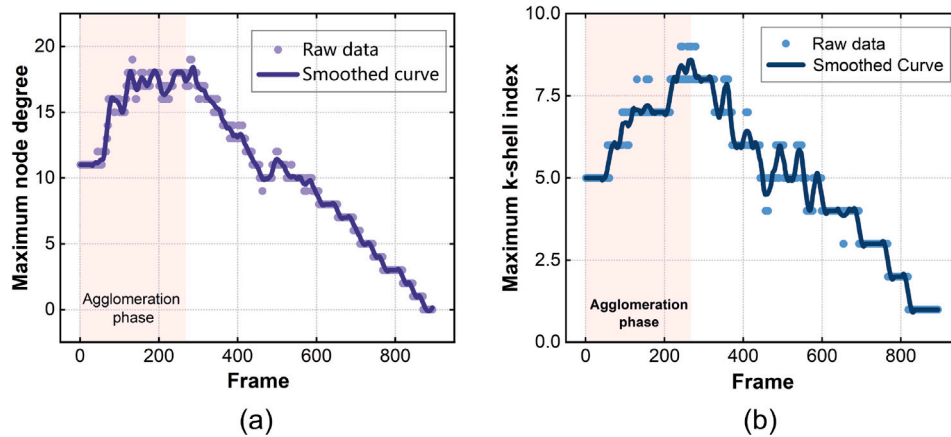
Fig. 16. Temporal evolutions of key-node metrics during evacuation experiments. (a) Maximum node degree as a function of time frame. (b) Maximum k-shell index as a function of time frame.

substantial portion of key nodes may reside outside these zones. Conversely, purely structural metrics (e.g., degree or k-shell) can capture network-bridging individuals but may neglect the context of local crowding. To address this limitation, we propose a hybrid, adaptive approach. First, the set of control nodes should be dynamically updated as the situation evolves, for example, by recomputing the centrality rankings at regular intervals to account for new arrivals or departures. Second, structural and density-based criteria should be jointly considered when selecting control points. One possible strategy is to prioritize nodes that score highly on a weighted index of degree (or k-shell) and local density. Another is to ensure that control nodes cover both dense cores and critical bridges, for instance, including some high

degree nodes from the densest zones and some high k-shell nodes near the periphery. As a result, an integrated strategy that updates control positions in real time and leverages both network topology and spatial density is expected to improve the robustness of crowd management and disturbance mitigation.

4. Conclusions

In this work, we demonstrate that proactive, network-targeted interventions can transform chaotic crowd evacuations back into orderly flow. Our dynamic-network simulations reveal that even a single perturbative event can trigger a sudden order–disorder phase transition,
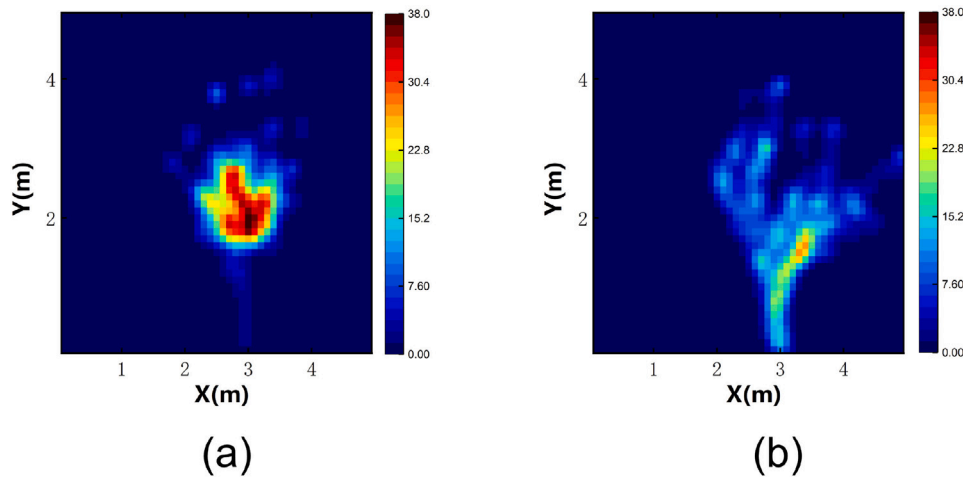
Fig. 17. Spatial distributions of key nodes during evacuation experiments. (a) Heatmaps of THD nodes. (b) Heatmaps of THK nodes.
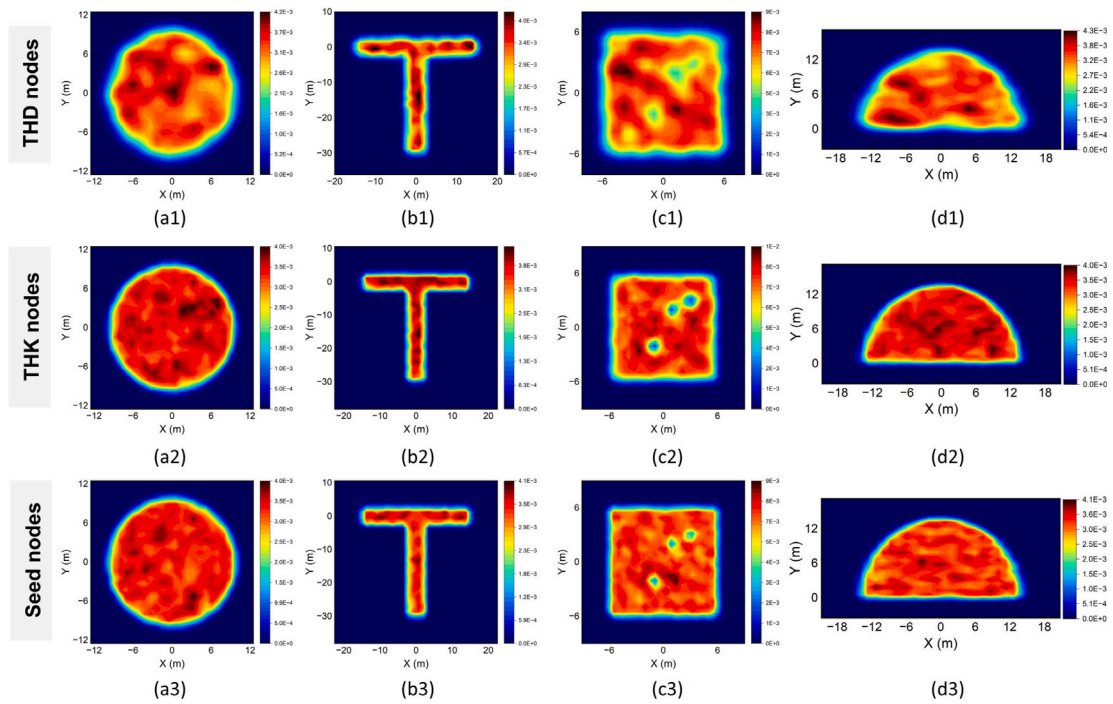

Fig. 18. Spatial distributions of key nodes across four typical architecture layouts. Columns (from left to right) correspond to the circular plaza (a*), T-shaped intersection (b*), obstacle room (c*), and semicircular hall (d*). Rows (from upper to bottom) distinguish THD nodes (a1–d1), THK nodes (a2–d2), and seed nodes (a3–d3).

yet directing a small subset of well-chosen individuals can effectively suppress this panic. Compared to random or density-based interventions, both high-degree and *k*-shell targeting significantly enhance evacuation performance by restoring alignment more quickly, reducing behavioral agitation, and requiring fewer controlled agents. In particular, high-degree targeting remains effective at higher crowd densities, whereas purely density-based control tends to overlook the majority of truly influential nodes.

These insights have important practical implications. First, evacuation planning should account for network topology — for example, placing security personnel or autonomous agents at hubs (e.g., focal gathering points or chokepoints) rather than solely at peaks of local density — and complementing physical guidance with positive-emotion cues (calming signals, trained pacers, informative messaging).

At the same time, real-time implementation faces sensing and latency constraints: estimating a live proximity network (wearables or vision) and refreshing centrality ranks introduce delays that can approach contagion time scales, thereby eroding the benefit of targeted control. In addition, our model does not include injury mechanics, fallen obstacles, or structural yielding [25,28], outflow and bottleneck effects emerge from social force interactions and geometry, but crush-dominated regimes are not represented, so clearance times may be optimistic under extreme crowd pressure.

In conclusion, our findings underscore a shift from reactive responses to anticipatory, topology-aware control. By quantifying how network-targeted interventions reshape transition dynamics, we provide a framework for planners and engineers to design smarter buildings and protocols. Future work will (i) integrate and benchmark low-latency sensing–analytics–actuation loops and quantify robustness

to latency and measurement noise, (ii) expand heterogeneity and multimodality (e.g., individual variability [46,47], mixed mobility modes [48]), and (iii) extend validation to larger scales and more complex geometries; incorporating obstruction and injury processes is also a priority to close the gap to crush-dominated scenarios.

CRediT authorship contribution statement

Wenfeng Yi: Writing – review & editing, Writing – original draft, Software, Methodology, Funding acquisition, Formal analysis, Data curation. **Wenhan Wu:** Writing – review & editing, Writing – original draft, Visualization, Validation, Supervision, Software, Methodology, Conceptualization.

Declaration of competing interest

The authors declare that they have no known competing financial interests or personal relationships that could have appeared to influence the work reported in this paper.

Acknowledgments

Data availability

Data will be made available on request.

References

[1] Weber CA, Bock C, Frey E. Defect-mediated phase transitions in active matter. Phys Rev Lett 2014;112(16):168301. http://dx.doi.org/10.1103/physrevlett.112.168301.

[2] Be'er A, Ilkanaiv B, Gross R, Kearns DB, Heidenreich S, Bär M, Ariel G. A phase diagram for bacterial swarming. Commun Phys 2020;3(1). http://dx.doi.org/10.1038/s42005-020-0327-1.

[3] Doha U, Aydin O, Joy MSH, Emon B, Drennan W, Saif MTA. Disorder to order transition in cell-ECM systems mediated by cell-cell collective interactions. Acta Biomater 2022;154:290–301. http://dx.doi.org/10.1016/j.actbio.2022.10.012.

[4] Xiao Y, Lei X, Zheng Z, Xiang Y, Liu Y-Y, Peng X. Perception of motion salience shapes the emergence of collective motions. Nat Commun 2024;15(1). http://dx.doi.org/10.1038/s41467-024-49151-x.

[5] Sayin S, Couzin-Fuchs E, Petelski I, Günzel Y, Salahshour M, Lee C-Y, Graving JM, Li L, Deussen O, Sword GA, Couzin ID. The behavioral mechanisms governing collective motion in swarming locusts. Sci 2025;387(6737):995–1000. http://dx.doi.org/10.1126/science.adq7832.

[6] Vicsek T, Czirók A, Ben-Jacob E, Cohen I, Shochet O. Novel type of phase transition in a system of self-driven particles. Phys Rev Lett 1995;75(6):1226–9. http://dx.doi.org/10.1103/physrevlett.75.1226.

[7] Buhl J, Sumpter DJT, Couzin ID, Hale JJ, Despland E, Miller ER, Simpson SJ. From disorder to order in marching locusts. Sci 2006;312(5778):1402–6. http://dx.doi.org/10.1126/science.1125142.

[8] Bacik KA, Sobota G, Bacik BS, Rogers T. Order–disorder transition in multidirectional crowds. Proc Natl Acad Sci 2025;122(14). http://dx.doi.org/10.1073/pnas.2420697122.

[9] He Z, Shen K, Lan M, Weng W. The effects of dynamic multi-hazard risk assessment on evacuation strategies in chemical accidents. Reliab Eng Syst Saf 2024;246:110044. http://dx.doi.org/10.1016/j.ress.2024.110044.

[10] Hoogendoorn SP. Pedestrian flow modeling by adaptive control. Transp Res Rec J Transp Res Board 2004;1878(1):95–103. http://dx.doi.org/10.3141/1878-12.

[11] Dang H-T, Gaudou B, Verstaevel N. A literature review of dense crowd simulation. Simul Model Pr Theory 2024;134:102955. http://dx.doi.org/10.1016/j.simpat.2024.102955.

[12] Bain N, Bartolo D. Dynamic response and hydrodynamics of polarized crowds. Sci 2019;363(6422):46–9. http://dx.doi.org/10.1126/science.aat9891.

[13] Chalons C. Numerical approximation of a macroscopic model of pedestrian flows. SIAM J Sci Comput 2007;29(2):539–55. http://dx.doi.org/10.1137/050641211.

[14] Aghamohammadi R, Laval JA. Dynamic traffic assignment using the macroscopic fundamental diagram: A review of vehicular and pedestrian flow models. Transp Res Part B: Methodol 2020;137:99–118. http://dx.doi.org/10.1016/j.trb.2018.10.017.

[15] Helbing D, Molnár P. Social force model for pedestrian dynamics. Phys Rev E 1995;51(5):4282–6. http://dx.doi.org/10.1103/physreve.51.4282.

[16] Helbing D, Farkas I, Vicsek T. Simulating dynamical features of escape panic. Nat 2000;407(6803):487–90. http://dx.doi.org/10.1038/35035023.

[17] Liu Y-C, Jafari A, Shim JK, Paley DA. Dynamic modeling and simulation of electric scooter interactions with a pedestrian crowd using a social force model. IEEE Trans Intell Transp Syst 2022;23(9):16448–61. http://dx.doi.org/10.1109/tits.2022.3150282.

[18] Ma Y, Yuen RKK, Lee EWM. Effective leadership for crowd evacuation. Phys A 2016;450:333–41. http://dx.doi.org/10.1016/j.physa.2015.12.103.

[19] Bosse T, Duell R, Memon ZA, Treur J, van der Wal CN. A multi-agent model for mutual absorption of emotions. In: Otamendi J, Bargiela A, Montes JL, Doncel Pedrera LM, editors. ECMS 2009 proceedings. ECMS; 2009, p. 212–8. http://dx.doi.org/10.7148/2009-0212-0218.

[20] Wang L, Short MB, Bertozzi AL. Efficient numerical methods for multiscale crowd dynamics with emotional contagion. Math Models Methods Appl Sci 2017;27(01):205–30. http://dx.doi.org/10.1142/s0218202517400073.

[21] Sosna MMG, Twomey CR, Bak-Coleman J, Poel W, Daniels BC, Romanczuk P, Couzin ID. Individual and collective encoding of risk in animal groups. Proc Natl Acad Sci 2019;116(41):20556–61. http://dx.doi.org/10.1073/pnas.1905585116.

[22] Poel W, Daniels BC, Sosna MMG, Twomey CR, Leblanc SP, Couzin ID, Romanczuk P. Subcritical escape waves in schooling fish. Sci Adv 2022;8(25). http://dx.doi.org/10.1126/sciadv.abm6385.

[23] van Haeringen ES, Veltmeijer EA, Gerritsen C. Empirical validation of an agent-based model of emotion contagion. IEEE Trans Affect Comput 2024;15(1):273–84. http://dx.doi.org/10.1109/taffc.2023.3272031.

[24] Wu W, Zheng X, Romanczuk P. Escape cascades as a behavioral contagion process with adaptive network dynamics. Phys Rev Res 2025;7(1):013300. http://dx.doi.org/10.1103/physrevresearch.7.013300.

[25] Guo C, Huo F, Li Y, Li C, Zhang J. An evacuation model considering pedestrian crowding and stampede under terrorist attacks. Reliab Eng Syst Saf 2024;249:110230. http://dx.doi.org/10.1016/j.ress.2024.110230.

[26] Kim G, Heo G. Agent-based radiological emergency evacuation simulation modeling considering mitigation infrastructures. Reliab Eng Syst Saf 2023;233:109098. http://dx.doi.org/10.1016/j.ress.2023.109098.

[27] Ding Z, Xu S, Xie X, Zheng K, Wang D, Fan J, Li H, Liao L. A building information modeling-based fire emergency evacuation simulation system for large infrastructures. Reliab Eng Syst Saf 2024;244:109917. http://dx.doi.org/10.1016/j.ress.2023.109917.

[28] Yang Y, Xie D-F, Zhao X-M, Jia B. Two-stage stochastic optimization of passenger evacuation routes in metro stations considering stampede incidents. Reliab Eng Syst Saf 2025;260:111047. http://dx.doi.org/10.1016/j.ress.2025.111047.

[29] Lu P, Li Y. Agent-based fire evacuation model using social learning theory and intelligent optimization algorithms. Reliab Eng Syst Saf 2025;260:111000. http://dx.doi.org/10.1016/j.ress.2025.111000.

[30] Hu Y, Li C, Ren X, Li H. The impact of a pedestrian obstacle at different times at the bottleneck on evacuation. Phys A 2025;660:130325. http://dx.doi.org/10.1016/j.physa.2024.130325.

[31] Xie C-ZT, Chen Q, Zhu B, Lee EWM, Tang T-Q, Yin X, Yuan Z, Zhang B. Coordinating dynamic signage for evacuation guidance: A multi-agent reinforcement learning approach integrating mesoscopic crowd modeling and fire propagation. Chaos Solitons Fractals 2025;194:116246. http://dx.doi.org/10.1016/j.chaos.2025.116246.

[32] Wang X, Zheng X, Cheng Y. Evacuation assistants: An extended model for determining effective locations and optimal numbers. Phys A 2012;391(6):2245–60. http://dx.doi.org/10.1016/j.physa.2011.11.051.

[33] Tian Z, Zhang G, Hong X, Lu D. Panic emotional contagion in emergencies: The role of safety and hazard information diffusion. Int J Disaster Risk Reduct 2025;116:105146. http://dx.doi.org/10.1016/j.ijdrr.2024.105146.

[34] Watts DJ, Strogatz SH. Collective dynamics of 'small-world' networks. Nat 1998;393(6684):440–2. http://dx.doi.org/10.1038/30918.

[35] Yi W, Wu W, Wang X, Wang E, Zheng X. Order–disorder phase transitions in front of the exit during human crowd evacuations. Transp Res Part C: Emerg Technol 2024;163:104649. http://dx.doi.org/10.1016/j.trc.2024.104649.

[36] Moussaïd M, Helbing D, Theraulaz G. How simple rules determine pedestrian behavior and crowd disasters. Proc Natl Acad Sci 2011;108(17):6884–8. http://dx.doi.org/10.1073/pnas.1016507108.

[37] Helbing D, Johansson A, Al-Abideen HZ. Dynamics of crowd disasters: An empirical study. Phys Rev E 2007;75(4):046109. http://dx.doi.org/10.1103/physreve.75.046109.

[38] van Haeringen E, Gerritsen C. Simulating panic amplification in crowds via density-emotion interaction. In: Proceedings of the 2023 international conference on autonomous agents and multiagent systems. 2023, p. 1895–902.

[39] Fredrickson BL. The role of positive emotions in positive psychology: The broaden-and-build theory of positive emotions. Am Psychol 2001;56(3):218–26. http://dx.doi.org/10.1037/0003-066x.56.3.218.

[40] Isen AM. Positive effect and decision making. Handb Emot 2000;417–35.

[41] Kitsak M, Gallos LK, Havlin S, Liljeros F, Muchnik L, Stanley HE, Makse HA. Identification of influential spreaders in complex networks. Nat Phys 2010;6(11):888–93. http://dx.doi.org/10.1038/nphys1746.

[42] He Y, Jin Y, Cao J, Sui S, Wang J, Ran B. Identification of key nodes in urban bus-metro network: A NK-shell algorithm based neighborhood KS. Reliab Eng Syst Saf 2025;264:111448. http://dx.doi.org/10.1016/j.ress.2025.111448.

[43] Yi W, Wu W, Wang X, Zheng X. Phase transitions in pedestrian evacuation: A dynamic modeling with small-world networks. IEEE Trans Intell Transp Syst 2024;25(11):18025–37. http://dx.doi.org/10.1109/tits.2024.3433420.

[44] Liu Y-Y, Slotine J-J, Barabási A-L. Controllability of complex networks. Nat 2011;473(7346):167–73. http://dx.doi.org/10.1038/nature10011.

[45] Lügering H, Sieben A. A rumor has spread like wildfire? - Empirical investigation of information propagation in waiting crowds. Collect Dyn 2024;9:1–28. http://dx.doi.org/10.17815/cd.2024.146.

[46] Wu W, Chen M, Li J, Liu B, Zheng X. An extended social force model via pedestrian heterogeneity affecting the self-driven force. IEEE Trans Intell Transp Syst 2022;23(7):7974–86. http://dx.doi.org/10.1109/tits.2021.3074914.

[47] Wu W, Li J, Yi W, Zheng X. Modeling crowd evacuation via behavioral heterogeneity-based social force model. IEEE Trans Intell Transp Syst 2022;23(9):15476–86. http://dx.doi.org/10.1109/tits.2022.3140823.

[48] Liu E, Barker K, Chen H. A multi-modal evacuation-based response strategy for mitigating disruption in an intercity railway system. Reliab Eng Syst Saf 2022;223:108515. http://dx.doi.org/10.1016/j.ress.2022.108515.